ELECTROMAGNETIC LITHIUM RING COMPRESSION FOR MAGNETIZED TARGET FUSION APPLICATION: SHELL BUCKLING

Fatemeh Edalatfar[1], Lemuel Santos[1], Hashem Jayhooni[1], Jean-Sebastien Dick[1]

[1]General Fusion Inc, Richmond, BC, Canada

ABSTRACT

Magnetized target fusion (MTF) relies on rapidly compressing magnetized plasma within a flux conserver to attain fusion conditions. Maintaining the smoothness and symmetry of the plasma-facing surface during compression is crucial, as any asymmetric deformation or buckling of the solid metal shell can disrupt magnetic confinement, reducing plasma temperature, and lifetime.

To establish the criteria for preventing buckling in solid ring implosions, we assess the effectiveness of the dynamic plastic flow buckling model. This assessment involves analyzing buckling phenomena in magnetically driven, imploding lithium rings. This investigation includes a total of 5 experiments with variations in collapse velocities, radius-to-thickness ratios, and initial ring temperatures. We capture and analyze the collapse trajectories and deformations of the rings during implosion using computer vision techniques. To establish material properties required for the theory, we utilize the Johnson-Cook model for the lithium ring with strain and strain rate extracted from the experiments. Using the extracted material properties and ring dimensions and employing the analytical model, we predict critical buckling velocities and dominant modes for each experimental scenario.

We observe qualitative agreement between the experiment and analytical model within measurement uncertainty, indicating the potential to define design, manufacturing, and quality requirements for larger-scale Magnetized Target Fusion experiments using solid shells to achieve fusion conditions.

Keywords: magnetized target fusion, dynamic stability, dynamic pulse buckling, plastic flow, strain hardening, magnetically-driven imploding rings

NOMENCLATURE

A Johnson-Cook initial Yield stress coefficient
B Johnson-Cook strain hardening stress coefficient
C Johnson-Cook rate hardening coefficient
E_h strain-hardening modulus/ tangent modulus
F_n buckling displacement FFT coefficient

I ring element moment of inertia per unit length
M bending moment
N thrust force
Q shear force
T Temperature
T_{melt} Johnson-Cook melting temperature
T_{ref} Johnson-Cook reference temperature

h ring thickness
h_0 ring initial thickness
m Johnson-Cook thermal softening power coefficient
$\acute{n}$ Johnson-Cook strain hardening power coefficient
n mode number
p normal force per unit length
r instantaneous radial location of the mid-surface of the shell element
r_0 initial radius of the mid-surface of the shell element
t time
$w(\theta,t)$ radially inward perturbation growth that arise during collapse
$w_i(\theta)$ initial perturbation of shell cross section from the circular form
$\dot{\varepsilon}$ Johnson-Cook reference strain rate
ε_p plastic strain
ε_e equivalent plane strain
ε_r radial strain
ε_θ tangential strain
κ curvature
$d\lambda$ arc length corresponding to $d\theta$
$d\varphi$ subtended angle of $d\theta$ at instantaneous center of curvature
$d\theta$ angle corresponding to the moving element of the ring
ρ density
$\bar{\sigma}$ average plastic flow stress

1. INTRODUCTION

Magnetized Target Fusion (MTF) is a technology that aims at reducing the cost to achieve fusion conditions for energy generation [1]. Among the different sub-technologies of MTF, the ones that rely on a magnetized plasma being compressed by a magnetic flux conserver are of particular interest because they rely on already available technologies. General Fusion Inc. aims to achieve nuclear fusion conditions by compressing a toroidal magnetized plasma through the implosion of a cylindrical solid lithium shell [2]. One of the main prerequisites for the successful implementation of this concept is the maintenance of magnetohydrodynamic (MHD) stability in the plasma throughout the compression process. One of the factors affecting the MHD stability is the evolution of flux-conserver geometry throughout the implosion [3]. Asymmetric deformation or buckling of the plasma-facing surfaces disrupts plasma magnetic confinement, reduces plasma temperature and plasma lifetime. Accordingly, studying circular cross-section shell implosions is essential to finding out the requirements to minimize dynamic instabilities and buckling in the plasma-facing surfaces.

High-speed collapse of shells with circular cross section has been investigated in literature for various applications. These applications include strain-rate dependent material properties identification experiments, explosive magnetic flux compression generators, and rapid gas-tight closing of pipes [4-5]. In all these devices, performance is optimized whenever buckling is absent during the collapse motion. Lindberg and Florence [6] has done an extensive analysis and experimentation in dynamic pulse buckling. They showed under long duration loads, buckling is elastic. It was demonstrated that under impulsive or nearly impulsive loads, the threshold for buckling can exhibit either elastic or plastic behavior, depending on the ratio of radius to thickness and the material model of the ring or shell [6]. Timoshenko developed the equations for elastic buckling of thin circular rings which is subjected to uniform radial pressure [7]. This analysis provides a connection between the applied external pressure and the specific buckling mode that appears on the ring shape. Based on the definitions provided in [6], the experiments conducted in this study are considered to involve thick rings, with buckling determined to be plastic.

The dynamic plastic buckling model for an imploding ring element was formulated considering various simplifying approximations through different research work [5-6,8-10]. The theory was derived based on the equation of motion for a uniform imploding ring element perturbed by either nonuniformity in the initial ring geometry or the radial imploding velocity. The theory predicts the growth of the buckles relative to the initial perturbation and identifies the most amplified buckling mode. According to the theory, it is possible to determine a critical velocity at which the amplification factor of the initial perturbations is less than a specific value [6].

In this work, our objective is to develop an analytical tool based on the theory on biaxial dynamic plastic flow buckling of rings during a radial impulse to guide our experimentation in electromagnetic-driven imploding lithium rings. The theoretical models are quite useful in informing the early-stage designs and at some points might be adequate for the final designs if the requirement of the theory is met. In contrast to higher fidelity numerical simulations, the analytical tool offers the advantage of significantly reduced computational costs, quicker calculations, and suitability for iterative design processes.

In Section 2 of this paper, the analytical modeling for lithium rings, based on the work of Lindberg and Florence [6], is explained. Section 3 describes the experimental apparatus. In Section 4, the theoretical analysis based on the material and geometrical properties for each experiment was presented. In this section, the experimental results are also summarized and compared against analytical results. The paper is concluded in the final section.

2. ANALYTICAL MODEL

As a perfectly circular ring is imploded using a perfect uniform velocity, the ring flows into a uniform cylindrical shell of smaller radius and thicker walls. In case of any perturbation either in geometry, material properties, and loading, a small part of the ring lags the rest of the ring. The compressive hoop stress, that develops during inward motion, amplifies the perturbation growth. For a perfectly plastic material, the steady increase of circumferential compressive strain at all points of the wall thickness implies an unchanging plastic flow stress. Accordingly, there is no bending moment to withstand the buckling and the converging motion would be unstable. However, for a viscoplastic material, the rate of circumferential strain is different at each side of the shell because of the difference in the amount of curvature. As shown in Fig. 1, the amount of strain growth in convex side of the perturbed shell element (point A) is smaller relative to the equivalent point on the concave side of the shell (point B). Accordingly, due to the difference between the circumferential stresses at points A and B, a bending moment will act on the section AB of the shell that resists buckling. As the collapse proceeds, the ring becomes thicker. Both the thrust stimulating buckling and the bending moment resisting buckling increases. However, the thrust is a function of thickness, but the bending moment is a function of thickness cubed. Accordingly, the ring stability improves. This means that the modes that are unstable at the beginning of the collapse can become stable as the collapse advances. Moreover, since the growth of the perturbations requires time, at high collapse velocities, the buckle sizes can stay within acceptable values [5-6]. The analytical calculations presented here are based on the theories developed by Lindberg and Florence [6] of plastic buckling of rings under dynamic radial loading. In this analytical model, the directional contribution to the restoring moment is neglected. In addition, the collapse velocity is considered constant which is another way to say that only a small amount of initial kinetic energy is absorbed by plastic work. The last assumption is that the deviation from circular form of the ring does not cause strain rate reversal throughout the motion.
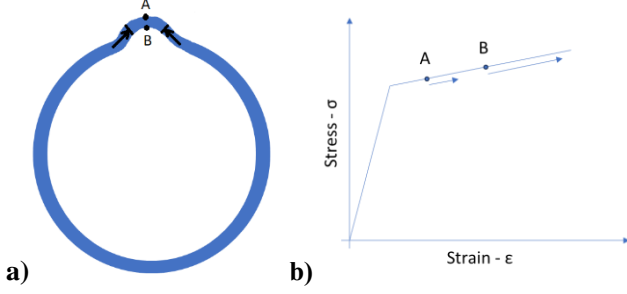
FIGURE 1. **a)** Growth of nonuniformity under hoop stress in contacting motion, **b)** Constant strain-hardening stress-strain relationship in a collapsing ring [6]

The equation of motion for a collapsing ring element can be derived using an element which is shown in Fig. 2. By neglecting rotary inertia, and by taking moments about any point on the element, per unit axial length we have:

$$Q = \frac{\partial M}{\partial \lambda} \tag{1}$$

The equation of motion for the radial motion of the collapsing shell is derived by summing up all radial forces. After simplifying, we get:

$$\frac{\partial Q}{\partial \lambda} + N \frac{\partial \varphi}{\partial \lambda} - p = \rho h \frac{\partial^2 (r-w)}{\partial t^2} \tag{2}$$

Considering the total inward displacement from a circle of radius $r(t)$ is $w(t, \theta) + w_i(\theta)$, the instantaneous curvature of the element is:

$$\kappa = \frac{1}{r(t)} + \frac{w(t,\theta) + \frac{\partial^2 w(t,\theta)}{\partial \theta^2} + w_i(\theta) + \frac{\partial^2 w_i(\theta)}{\partial \theta^2}}{r^2} \tag{3}$$

Considering $\kappa = \partial \varphi / \partial \lambda$, and given the relatively small values of both w and w_i relative to $r(t)$, which leads to $d\lambda \sim rd\theta$, and $N/r = \rho h\, \partial^2 r / \partial t^2 + p$, Eqn. (2) can be reformulated as:

$$\frac{1}{r^2} \frac{\partial^2 M}{\partial \theta^2} + \frac{N}{r^2} \left(w(t,\theta) + \frac{\partial^2 w(t,\theta)}{\partial \theta^2} + w_i(\theta) + \frac{\partial^2 w_i(\theta)}{\partial \theta^2} \right) = -\rho h \frac{\partial^2 w}{\partial t^2} \tag{4}$$

Solution of Eqn. (4) requires the values for restoring moment, M, and thrust force, N. In the absence of strain-rate reversal across a cross-section of the shell, the moment can be approximated based on pure elastic motion. The key distinction involves substituting the elastic modulus, E, with tangent modulus, E_h:

$$M = E_h I (\kappa - \kappa_i) \tag{5}$$

Which for a unit length of the shell, $I = h^3/12$. The thrust force for the element, would be the hoop stress times the area which is:
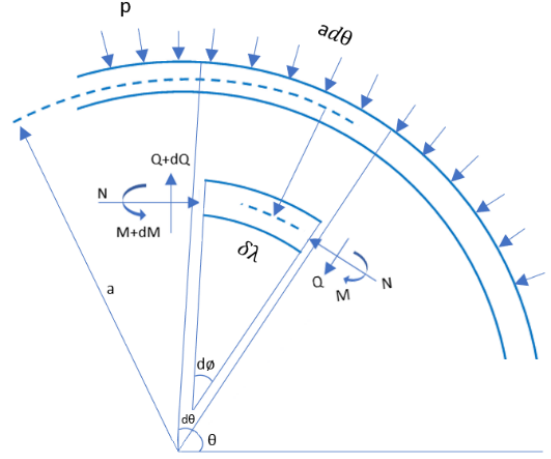
$$N = \bar{\sigma} h \tag{6}$$

FIGURE 2. Element of a ring in collapsing motion [6]

If we represent the buckling displacement and initial geometrical perturbation from circularity as:

$$w(\theta, t) = r_0 \sum_{n=2}^{\infty} [F_n(t) \cos n\theta + G_n(t) \sin n\theta] \tag{7}$$
$$w_i(\theta) = r_0 \sum_{n=2}^{\infty} [A_n \cos n\theta + B_n \sin n\theta] \tag{8}$$

Equation (4) becomes:

$$\rho \frac{\partial^2 f_n}{\partial t^2} + f_n (n^2 - 1) \left(\frac{E_h h^2 n^2}{12 r^4} - \frac{\bar{\sigma}}{r^2} \right) - \frac{\bar{\sigma}}{r^2} (n^2 - 1) = 0 \tag{9}$$

In the above equation, $f_n = F_n(t)/A_n$ is the amplification function. As long as the coefficient of f_n in Eqn. (9) remains positive, there won't be significant amplification in the growth of the amplification function. That means as long as

$$n > \sqrt{\frac{12 r^2 \bar{\sigma}}{E_h h^2}} \tag{10}$$

the collapse will remain stable. An additional insight from this equation is that the stability limit on the buckling mode number is proportional to radius and inversely proportional to thickness. Accordingly, as the radial inward motion progresses, the modes that may be initially unstable will eventually become stable.

For solving Eqn. (9), it is required to consider a material model for the lithium rings. The mechanical properties for the lithium ring that were used in analytical modeling and experiment is summarized in Tab. 1. For the lithium ring, a Johnson-Cook material model, Eqn. (11), was used to capture the flow stress dependence on strain hardening, strain-rate hardening and thermal softening:

$$\sigma = \left[A + B \left(\varepsilon_p \right)^{\acute{n}} \right] \left[1 + C \ln \left(\frac{\dot{\varepsilon}}{\dot{\varepsilon}_0} \right) \right] \left[1 - T^{* \, m} \right] \tag{11}$$

The definition of each material constant and other properties used in the study can be found in Tab. 1. The parameter T^* is the

homologous temperature $(T^*=(T - T_{ref})/(T_{melt} - T_{ref}))$. Further details on these parameters can be found in Miao Y. [11]. Using the material model and for each experiment, Eqn. (9) was solved numerically using Runge-Kutta method. The experimental and analytical results are discussed in the next section.

**TABLE 1.** Recycled lithium mechanical properties

| Density, ρ (kg/m³)	530
Elastic Modulus, E (GPa)	7.82
Poisson Ratio	0.48
Initial Yield, A (MPa)	0.744
Hardening Constant, B (MPa)	19.8
Hardening Exponent, n	0.3
Reference Strain Rate, $\dot{\varepsilon}_0$	0.002
Strain Rate Constant, C	0.0141
Thermal Softening Exponent, m	0.77
Melting Temperature, T_{melt} (°C)	180
Reference Temperature, T_{ref} (°C)	21

3. EXPERIMENTAL APPARATUS

The objective of the experiment is to study and characterize the buckling behavior of a lithium ring in response to the magnetically induced dynamic compressive loading. A solid lithium ring is placed inside a custom-made aluminum solenoid connected to high-voltage power supply as shown in Fig. 3. Electromagnetic compression is achieved by applying a high-voltage capacitor discharge into the solenoid, creating an electromagnetic field that induces an impulsive force in the ring. High speed cameras (Photron FASTCAM Nova S12), at a frame rate of 22500 frames per second (FPS), were used to track the implosion and buckling behavior of the lithium ring. The high-speed camera footage was processed to extract the liner position and demonstrate the liner buckling behavior throughout the compression process. The images recorded provide a basis for the experimental observations and measurements, from which theories will be compared. Further details on the experimental apparatus parameters can be found in Dick et al. [2].

4. RESULTS AND DISCUSSION

In this section we describe and analyze the two sets of dynamic buckling experiments that have been conducted using recycled lithium rings. The dynamic loading for the collapse of the rings is created via electromagnetic induction following a rapid discharge of charge stored in capacitors. The solenoid is designed with a sliding fit tolerance for the rings in a way that the internal diameter of the solenoid equals the external diameter of the ring plus 6mm. The typical ring specimen has an external diameter of 527 mm.
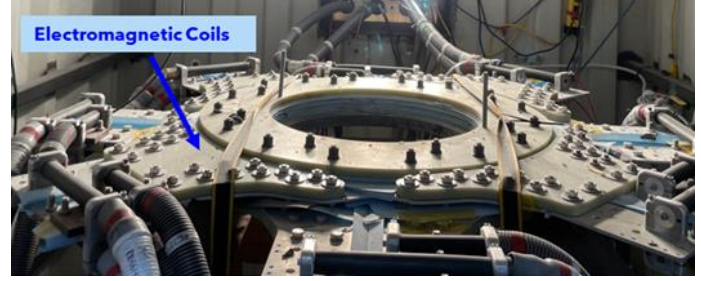
(a)
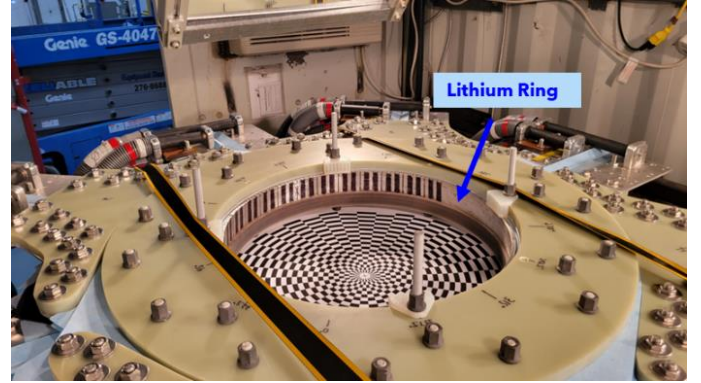
(b)

FIGURE 3. Experimental setup for lithium ring implosion showing **a)** electromagnetic coil and **b)** lithium ring

The rings thickness, height, temperature, and collapse velocity are shown in Tab. 2. Radius over thickness ratio for set A and set B of the experiment is roughly equal to 10 and 45, respectively.

TABLE 2. Summary of the experiments' conditions

Shot No.	Shot Conditions				
	Nominal OD (mm)	Ring Thickness (mm)	Height (mm)	Temperature (C)	Approximate Collapse Velocity (m/s)
1A	527	25.0	55.0	25	~91
2A	527	25.2	53.4	40	~192
3A	527	24.5	53.0	100	~213
1B	527	5.7	55.4	25	~332
2B	527	5.5	27	25	~620

Figure 4.a displays the top and side views of set A rings for each experiment after the collapse, and Fig. 4.b shows a snapshot of the set B experiment during the collapse. Set B experiments shattered into pieces at the end of the implosion, leaving nothing for preview after the collapse.
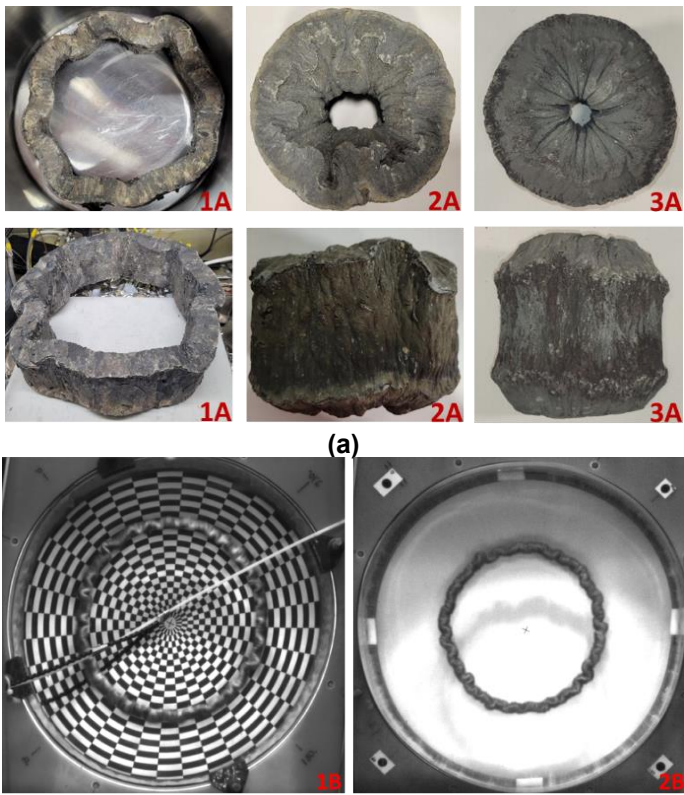
(a)

(b)

FIGURE 4. a) Top and side views of set A rings experiment, and **b)** Top view of set B rings during implosion

Figure 5 shows the trajectory of the mid-surfaces of the rings for set A and B experiments, respectively. A constant collapse velocity was extracted by fitting a line to these graphs. An upper limit of ∓5mm uncertainty was present in extracting the edges using image processing techniques.
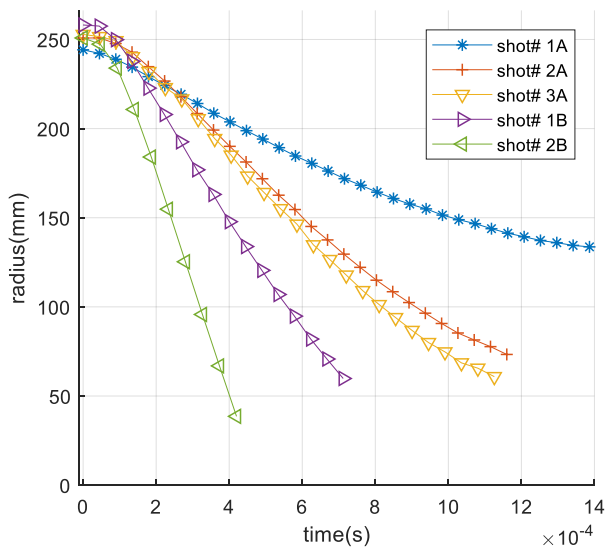

FIGURE 5. Experimental trajectories for rings collapse

Figure 6.a and b show the polar plot of the growth of the buckles on the inner edge of the rings during implosion in shot#1A and shot#1B, respectively. The amplification of the wrinkles can be followed in these set of plots. Based on the camera's FPS, the time difference between each consecutive graph is 44µs. According to Fig. 6 The number of crests in Shot#1A and Shot#1B are roughly ~8, and ~30, respectively.
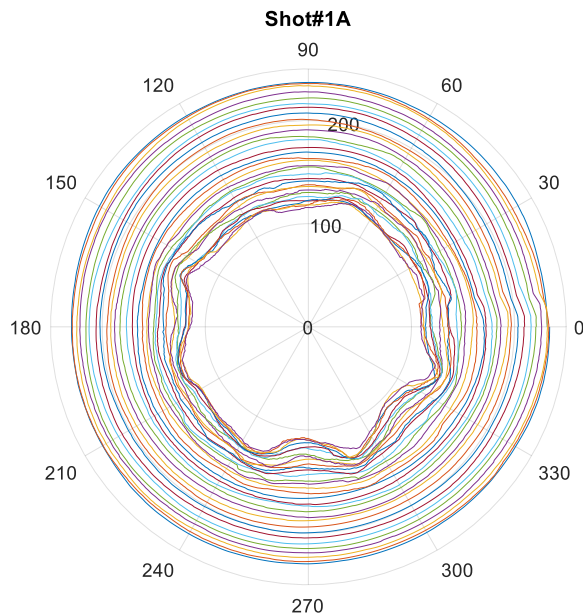
(a)
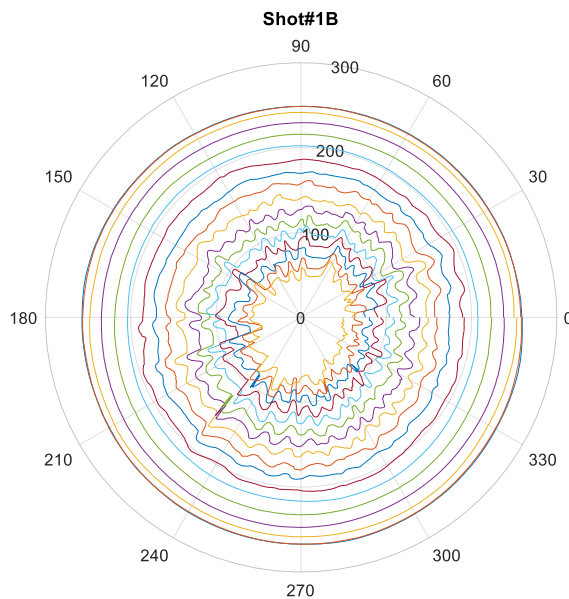
(b)

FIGURE 6. a) shot#1A, and **b)** shot#1B wrinkles growth evolution through time.

To solve Eqn. (9) for the performed experiments, it is necessary to input plastic stress ($\bar{\sigma}$) and strain hardening (E_h) into this equation. To achieve this, for each experiment, the strain and strain rate was extracted from the experimental liner trajectories. The equivalent plane strain is calculated based on Eqn. (12).

$$\varepsilon_e = \frac{1}{1+\upsilon}\sqrt{\varepsilon_r{}^2 - \varepsilon_r\varepsilon_\theta + \epsilon_\theta{}^2} \qquad (12)$$

where $\varepsilon_r = \frac{h_0-h}{h_0}$ and $\varepsilon_\theta = \frac{r_0-r}{r_0}$ are radial and circumferential strain, respectively. The temperature is also determined based on the initial temperature of the ring in each experiment. These values were then implemented into the Johnson-Cook model, and the values of $\bar{\sigma}$ and E_h were derived. Fig. 7 displays these values throughout the experiment. The data was magnified for the mid-range of the collapse where the collapse velocity is constant. As the ring temperature increases, strain hardening and flow stress decreases. Moreover, the strain-hardening value is almost constant throughout compression.
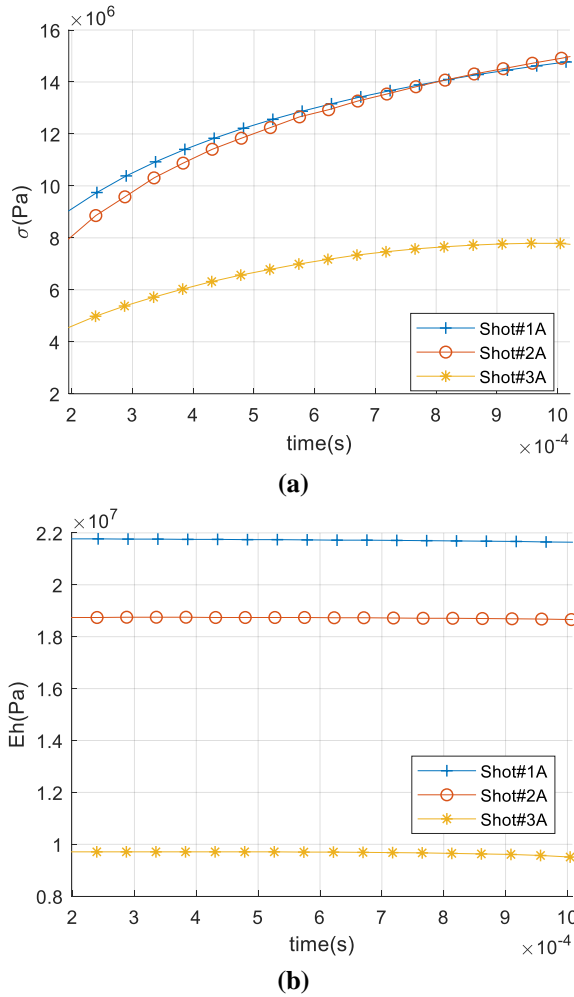

(a)

(b)

FIGURE 7. a) plastic flow stress, and **b)** strain hardening for set A of the experiments.

The solution to Eqn. (9) strongly depends on strain hardening, average flow stress, ring initial radius, and ring initial thickness. Equation 9 was solved using the average extracted values of $\bar{\sigma}$ and E_h for material and geometrical properties of shot #1A at different velocities and for the first 20 mode numbers. Figure 8 depicts the amplification factor versus velocity, extracted at the point where the growth type for that specific mode number, transitions from unstable to stable, i.e., when the coefficient of f_n in Eqn. (9) becomes positive. As evident from the Fig. 8, an increase in the collapse velocity significantly decreases the amplification factor. In this figure, the topmost graph in the group of diagrams corresponds to the dominant mode number.

Figure 9 illustrates the amplification factor versus mode numbers across a range of velocities, extracted based on the material and geometrical properties of shot #1A. The dominant mode number at all the velocities is observed to be 9 and counting the crests on Fig. 6.a for shot #1A results in approximately the same value. The theory can provide a rough prediction for both the dominant mode number and the velocity required to keep the amplification factor below a desired specific limit.

The same procedure was repeated for set B of the experiments. Due to the higher radius-to-thickness ratio in set B, the dominant mode shows higher values, as evident in the corresponding experimental results illustrated in Fig. 6.b. Figure 10 and 11 shows the amplification factor vs velocity, and amplification factor vs. mode number for Shot #2B, respectively. By comparing the approximate number of crests in Fig. 6.b, it can be observed that the theory predicts the dominant mode number with sufficient proximity to the experimental values.
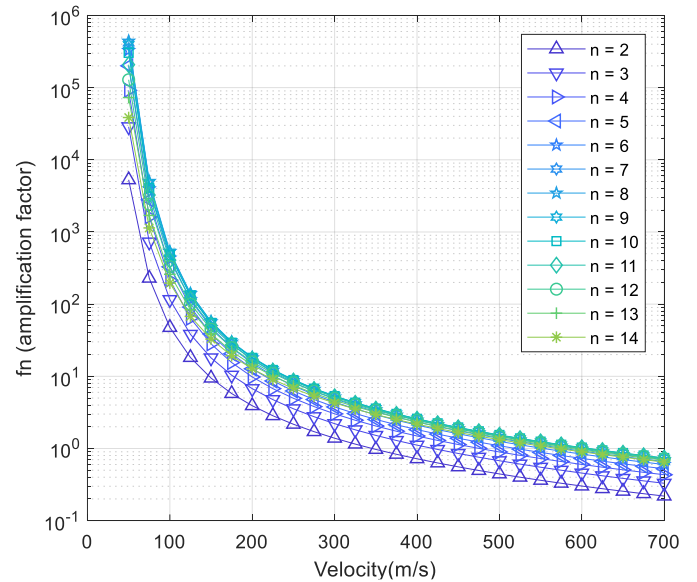

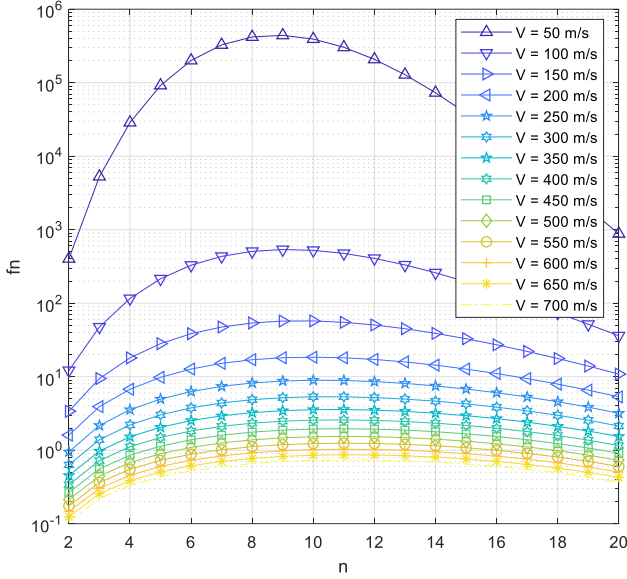**FIGURE 8.** Amplification factor vs. velocity solved for material and geometrical properties of Shot#1A

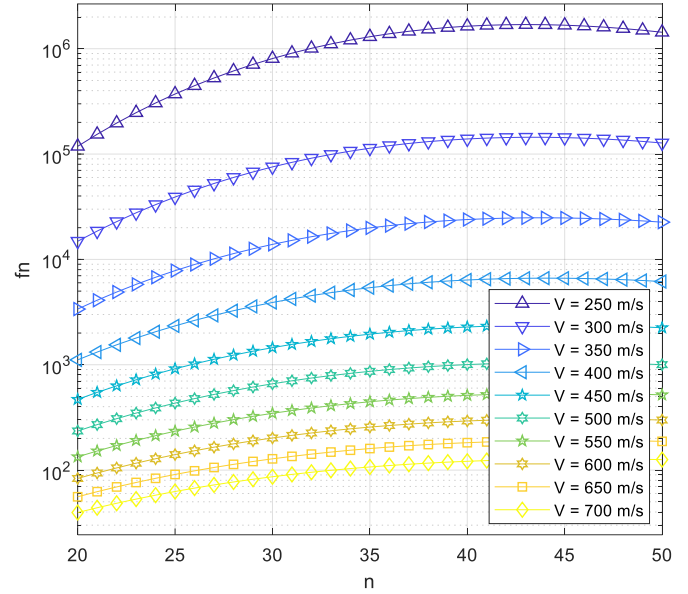**FIGURE 9.** Amplification factor vs. mode number solved for material and geometrical properties of Shot#1A

FIGURE 11. Amplification factor vs. mode number solved for material and geometrical properties of Shot#1B
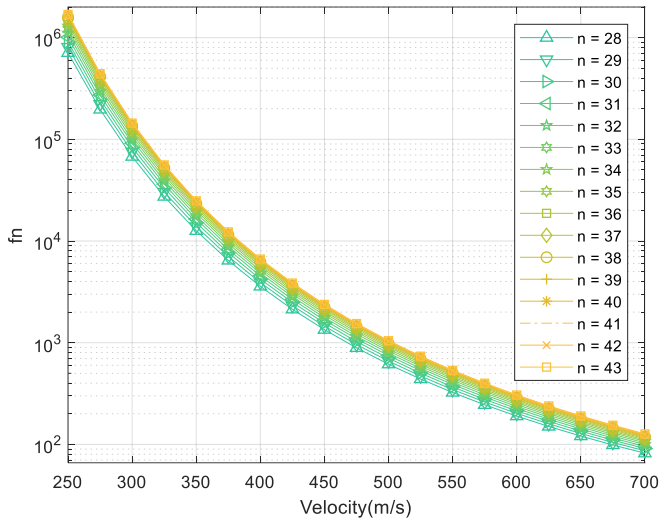

FIGURE 10. Amplification factor vs. Velocity solved for material and geometrical properties of Shot#1B

A precise comparison between the experiment and theory is challenging because the nonuniformities in the experimental velocity distributions and initial geometrical perturbation, which are necessary for the theory, are unknown. Instead, the study compares the observed number of crests which is interpreted as dominant mode numbers, with a theoretical limit which is dependent on the dimensions and material properties of the ring. The dominant mode number is unaffected by the geometrical and velocity nonuniformities. However, the absolute maximum imperfection growth which is seen in experiment is the product of initial imperfection of each mode times its amplification factor. Accordingly qualitative comparisons of experimental and theoretical mode numbers are done. Table 3 summarizes and compares the results from the analytical solution and experimental observations for all the experiments. From this table, it can be readily concluded that an increase in temperature, leading to the softening of the material, decreases the amplification factor and improves dynamic stability. In addition, increasing the collapse velocity improves stability. The mechanism by which increasing velocity helps stabilize the collapse is that wrinkles do not have enough time to grow within the implosion time.

TABLE 3. Summary of the experimental and analytical results

	Experimental Dominant Mode Number	Analytical Dominant Mode Number	Maximum Analytical Amplification Factor at the Experimental Velocity	Strain Hardening (E_h) [Pa]	Plastic flow stress $(\bar{\sigma})$ [Pa]	Mid Radius-to-Thickness Ratio
1A		7 to 8	75 to 1500	2.20e7	9e6 to 15e6	9.8
2A	~8 to ~10	7 to 10	6 to 40	1.90e7	8e6 to 15e6	9.9
3A		9 to 11	5 to 15	0.96e7	5e6 to 8e6	10.3
1B	~ 30	30 to 44	125 to 80000	2.20e7	8e6 to 18e6	45.3
2B	~ 44	42 to 52	200 to 8000	2.25e7	16e6 to 27e6	45.6

5. CONCLUSION

In this study, we conducted analytical modeling to explore the plastic dynamic pulse buckling of viscoplastic rings subjected to the radial force induced by a poloidal magnetic field. Two sets of experiments were carried out with radius-to-thickness ratios of approximately 10 and 45. Throughout these experiments, we varied the implosion velocity and rings initial temperature, investigating their impact on the dominant mode number of buckling and the amplification of the buckles. By comparing experimental results with analytical modeling, we concluded that the theory is reliable in predicting the limit of the dominant mode number. Furthermore, the theory can anticipate critical velocities where the amplification factor of the buckles is below a specific threshold. This fulfills our goal of establishing an analytical tool for estimating the dominant mode number and the necessary velocity to minimize buckle growth during the implosion. Accordingly, the analytical tool has the potential to define design, manufacturing, and quality requirements for larger-scale Magnetized Target Fusion experiments.

REFERENCES

[1] Wurden, Glen A., Scott C. Hsu, Tom P. Intrator, T. C. Grabowski, J. H. Degnan, M. Domonkos, P. J. Turchi et al. "Magneto-inertial fusion." Journal of Fusion Energy 35 (2016): 69-77.

[2] Dick, J.-S., Sirmas, N., Bernard, S., Santos, L., Forynski, P. (2024) "Electromagnetic Lithium Ring Compression for Magnetized Target Fusion Application: Trajectories." Pressure Vessels and Piping Conference 2024. American Society of Mechanical Engineers.

[3] Ishino, S. "Fusion Reactors (Magnetically Confined)-Tokamaks: Materials." Encyclopedia of Materials: Science and Technology (2001): 3422-3430.

[4] Duffey, T. A., R. H. Warnes, and J. M. Greene. "Growth of buckling instabilities during radial collapse of a ring." (1990): 145-151.

[5] Florence, A. L., and G. R. Abrahamson. "Critical velocity for collapse of viscoplastic cylindrical shells without buckling." (1977): 89-94.

[6] Lindberg, Herbert E., and Alexander L. Florence. Dynamic pulse buckling: theory and experiment. Vol. 12. Springer Science & Business Media, 2012.

[7] Timoshenko, Stephen P., and James M. Gere. Theory of elastic stability. Courier Corporation, 2009.

[8] Jones, Norman, and D. M. Okawa. "Dynamic plastic buckling of rings and cylindrical shells." Nuclear Engineering and Design 37, no. 1 (1976): 125-147.

[9] Al-Hassani, S. T. S. "The plastic buckling of thin-walled tubes subject to magnetomotive forces." Journal of Mechanical Engineering Science 16, no. 2 (1974): 59-70.

[10] Mainy, Aurélien. "Dynamic buckling of thin metallic rings under external pressure." (2012).

[11] Miao, Y., Sexsmith, M., Hartono, S., Preston, C., Tsai, B. and Sirmas, N. "Strain-rate-Dependent Parameters of Lithium as a Plasma Facing Material for Magnetized Target Fusion Application." Pressure Vessels and Piping Conference 2024. American Society of Mechanical Engineers.